A Comparative Evaluation of Snowflake Particle Size and Shape Estimation Techniques used by the Precipitation Imaging Package (PIP), Multi-Angle Snowflake Camera (MASC), and Two-Dimensional Video Disdrometer (2DVD)

Charles N. Helms[1,2], S. Joseph Munchak[1], Ali Tokay[1,3], and Claire Pettersen[4]

[1]Mesoscale Atmospheric Processes Laboratory, NASA Goddard Space Flight Center, Greenbelt, MD, USA
[2]NASA Postdoctoral Program—Universities Space Research Association, Columbia, MD, USA
[3]Joint Center for Earth Systems Technology, University of Maryland, Baltimore County, Baltimore, MD, USA
[4]Climate and Space Sciences and Engineering Department, University of Michigan, Ann Arbor, MI, USA

Correspondence: Charles N. Helms (charles.n.helms@nasa.gov)

Abstract. Measurements of snowflake particle size and shape are important for studying the snow microphysics. While a number of instruments exist that are designed to measure these important parameters, this study focuses on the measurement techniques of three digital video disdrometers: the Precipitation Imaging Package (PIP), the Multi-Angle Snowflake Camera (MASC) and the Two-Dimensional Video Disdrometer (2DVD). To gain a better understanding of the relative strengths and

5 weaknesses of these instruments and to provide a foundation upon which comparisons can be made between studies using data from different instruments, we perform a comparative analysis of the measurement algorithms employed by each of the three instruments by applying the algorithms to snowflake images captured by PIP during the ICEP-POP 2018 field campaign.

Our analysis primarily focuses on the measurements of area, equivalent diameter, and aspect ratio. Our findings indicate that area and equi-area diameter measurements using the 2DVD camera setup should be the most accurate, followed by MASC,

10 which is slightly more accurate than PIP. In terms of the precision of the area and equi-area diameter measurements, however, MASC is considerably more precise than PIP or 2DVD, which provide similar precision once the effects of the PIP image compression algorithm are taken into account. Both PIP and MASC use shape-fitting algorithms to measure aspect ratio. While our analysis of the MASC aspect ratio suggests the measurements are reliable, our findings indicate that both the ellipse and rectangle aspect ratios produced by PIP under-performed considerably due to the shortcomings of the PIP shape-

15 fitting techniques. That said, we also demonstrate that reliable measurements of aspect ratio can be retrieved from PIP by reprocessing the PIP images using either the MASC shape-fitting technique or a tensor-based ellipse-fitting technique. Because of differences in instrument design, 2DVD produces measurements of particle horizontal and vertical extent rather than length and width. Furthermore, the 2DVD measurements of particle horizontal extent can be contaminated by horizontal particle motion. Our findings indicate that, although the correction technique used to remove the horizontal motion contamination

20 performs remarkably well with snowflakes despite being designed for use with rain drops, the 2DVD measurements of particle horizontal extent are potentially unreliable.

1 Introduction

Digital video disdrometers have been in use since the 1990's and there exist several instruments designed around using digital cameras to observe precipitation properties. The measurements from these instruments are not only critical for understanding
25 precipitation microphysics but are also critical for developing algorithms to retrieve microphysical properties using radar and passive microwave sensor data. Due to the variety of instruments available, issues can arise when making comparisons between studies and algorithms that are based on data from different instruments. To this end, the present study will perform a comparison of the particle area, equivalent diameter, and aspect ratio measurements produced by three common ground-based digital video disdrometers: the Precipitation Imaging Package (PIP; Pettersen et al., 2020, 2021), the Multi-Angle Snowflake
30 Camera (MASC; Garrett et al., 2012), and the Two-Dimensional Video Disdrometer (2DVD; Kruger and Krajewski, 2002; Schönhuber et al., 2007, 2008).

Studies invoking snowflake particle size frequently rely on either the maximum dimension length of a particle (e.g., Locatelli and Hobbs, 1974; Heymsfield and Westbrook, 2010), typically defined as either the major-axis length of a fitted ellipse or as the diameter of the smallest circumscribing circle, or on the equivalent diameter (e.g., Han and Braun, 2021; Pettersen et al.,
35 2020, 2021), defined as the diameter of a circle or sphere with equal projected area (for the equi-area diameter) or volume (for the equi-volume diameter) to a particle. 2DVD combines orthogonal measurements of a particle to estimate the particle volume, from which the equi-volume diameter is computed while both PIP and MASC compute the equi-area diameter from their respective area measurements, both of which are determined by counting the number of pixels within the particle. That said, there have been efforts to use the multiple cameras mounted by MASC to compute particle volume (Leinonen et al.,
40 2021).

There are numerous examples of studies which rely heavily on either of these measures of particle size. For example, Han and Braun (2021) characterize the global three-dimensional distribution of precipitation mean particle sizes using satellite radar data; they used a form of the equivalent diameter as their metric of particle size, specifically the mass-weighted mean liquid-water-equivalent diameter. As with many studies that invoke particle size distributions, their choice of metric came down to the
45 choice of metric used in the original particle size distribution parameterization. For Han and Braun (2021), the authors used data produced following Grecu et al. (2016), which used the particle size distribution parameterization described in Testud et al. (2001). Testud et al. (2001) chose to base their parameterization on equivalent diameter, specifically the volume-weighted mean liquid-water-equivalent diameter, for two key reasons: the authors argue that this variable has less physical ambiguity than other metrics and is relatively easy to compute.

50 The equivalent diameter measurements have also been used to determine a number of bulk snowflake characteristics. Pettersen et al. (2020) used PIP-observed equivalent diameter measurements to compare a number of microphysical and bulk characteristics of snow, including the liquid-water-equivalent snow rate and the bulk effective density of the snow particles, to collocated observations. Their study found that the liquid-water-equivalent snow rate compared very well to both established retrievals as well as observations. Using these bulk characteristics, Pettersen et al. (2021) was able to discriminate between
55 different precipitation phases using the PIP observations.

Empirical relationships between snowflake or ice crystal size and terminal fall speed frequently use the maximum dimension of the particle as their independent variable (e.g., Locatelli and Hobbs, 1974). The more advanced relationships also incorporate the Reynolds number, which is dependent on the particle area exposed to the flow via the Best number; in some cases this area is replaced by an area ratio that is defined as the ratio between the area exposed to the flow and the area of the circumscribing

60 circle, which is a function of the particle maximum dimension (Heymsfield and Westbrook, 2010). In this way, the terminal fall speed relationships can depend on both the equivalent diameter, which is directly tied to particle area, and the maximum dimension of the particle. Similarly, combinations of equivalent diameter and maximum dimension have also been used to estimate particle mass (e.g., von Lerber et al., 2017).

Snowflake shape, separate from the snowflake size, is generally characterized by the aspect ratio of the snowflakes. Korolev

65 and Isaac (2003) found that the mean aspect ratio of in-cloud ice particles varied as a function of the particle maximum dimension for particles smaller than ~65 μm whereas the aspect ratio of larger particles (i.e., those typical of snow) tended to vary inversely with temperature; the mean aspect ratios observed by the study were between 0.6 and 0.8 with the snowflake-sized particles tending to have mean aspect ratios closer to 0.6. To constrain radar backscatter calculations, aspect ratio is frequently prescribed, often with a mean value of 0.6 assumed (e.g., Matrosov et al., 2005), although a number of studies

70 have performed backscatter calculations using a range of prescribed aspect ratios (e.g., Tyynelä et al., 2011; Westbrook, 2014). The reverse of this process has also been attempted: Munchak et al. (2021) used an optimal estimation technique to retrieve a number of snow microphysical properties, including aspect ratio, from a dual-frequency dual-polarization ground-based radar, albeit with mixed results.

The goal of the present study is to evaluate the techniques used by each of the three ground-based digital video disdrometers

75 to determine the size and shape of precipitation particles in terms of the area, equivalent diameter, and aspect ratio. In doing so, we will provide a point of comparison for these three sensors. The next section will briefly discuss the data sets used for this study. In section 3, we will provide a detailed description of each sensor and their respective processing algorithms as they relate to the particle shape. This will be followed by a description of our analysis methods in section 4. Section 5 will present the results of our study. Finally, section 6 will present our conclusions alongside a brief summary of the study.

80 ## 2 Data

The data sets used to perform the analyses central to this study were collected during the 2018 International Collaborative Experiment for PyeongChang Olympic and Paralympics (ICE-POP; Lee and Kim, 2019; Lim et al., 2020; Tapiador et al., 2021). ICE-POP, which took place between 1 November 2017 and 17 March 2018, was an international collaboration between a number of programs and agencies, including the NASA Global Precipitation Mission (GPM) Ground Validation program and

85 the Korean Meteorological Administration (KMA). The field campaign was designed to study winter precipitation in complex terrain and involved a number of measurement sites featuring a mixture of in-situ and remote-sensing instrumentation. Of interest to the present study is the May Hills supersite (MHS; 37.6652°N, 128.6996°E) as this site has collocated PIP, MASC, and 2DVD instruments and experienced frequent snow events. This study will focus on data collected during a snow event that

took place on 7–8 March 2018. This event was selected as it contains both aggregate snow particles, which provide a large
90 variety of shapes (and, therefore, aspect ratios), and lump graupel particles, which tend to be relatively spherical with high
aspect ratios.

3 Instruments

This study will evaluate the measurement techniques of three video disdrometers: PIP, MASC, and 2DVD. The instruments
and their processing algorithms, as they relate to measuring the shape and orientation of snow particles, will be covered in this
95 section.

3.1 Precipitation Imaging Package (PIP)

PIP (Pettersen et al., 2020, 2021) is a video disdrometer developed by NASA as a successor to the Snowflake Video Imager
(SVI; Newman et al., 2009). PIP is composed of two parts: a high-speed video camera and a light source to backlight the
precipitation particles that pass through the open sampling volume. The camera, of the 'charge-coupled device' (CCD) variety
100 and located 2 m from the light source, continuously records images at a rate of 380 frames per second as 640 by 480 pixel
images with a resolution of 0.1 mm by 0.1 mm using a focal plane located 1.33 m away from the camera. In order to reduce the
data rate produced by the high speed camera, the PIP images are compressed before being processed, resulting in an effective
resolution of 0.1 mm in the horizontal by 0.2 mm in the vertical.

  The PIP processing algorithms are written using the IMAQ Visual software package (National Instruments, 2000), a software
105 package designed for use in performing automated quality control of manufacturing processes. Of particularly interest to the
present study are the methods the algorithm uses to compute the dimensions of the precipitation particle. While particle area
is determined by counting the number of pixels within the particle, the particle dimensions are determined by fitting an ellipse
or a rectangle to the particle as viewed by PIP, which sees the two-dimensional projection of the particle, after the PIP image
has been compressed to reduce data rates. The IMAQ software package performs both the ellipse and rectangle fitting by
110 constructing an ellipse or rectangle that has an equal area and an equal perimeter to the target particle; a derivation of the
equations used to make these fits are presented in Appendix A to supplement the limited information given in the IMAQ
manual. The long and short axes of the fitted shapes are then used as the length and width of the particle. Specifically, the
ellipse fit produces the variables 'Ellip_Maj' and 'Ellip_Min' for the length and width, respectively, while the rectangle fit
produces the variables 'Rec_BS' and 'Rec_SS' for the length and width, respectively. Note, in both the ellipse and rectangle
115 fits, the perimeter and area are defined such that any holes in the particle are not taken into account. Because of this, the PIP-
determined area and perimeter of a particle with no holes will be the same as an otherwise-identical particle with a hole when
determining the shape fits.

3.2 Multi-Angle Snowflake Camera (MASC)

MASC (Garrett et al., 2012) is another video disdrometer and was developed at the University of Utah; the setup described
below is that used during the ICE-POP field campaign. Unlike PIP, MASC employs three cameras and only records images
when triggered by a particle falling through the field of view of a pair of near-infrared sensors. The near-infrared sensors are
also used to trigger a flash, which illuminates the particle from the side facing the cameras. The three cameras, also of the CCD
variety and separated from one another by 36°, are mounted looking into an enclosed sampling volume, open only at the top
and bottom, and have a common focal point 10 cm away from each lens. Typically, the camera system is artificially restricted to
only being triggered once per second in order to reduce excessive flashes. The sampling volume is defined by the intersection
of the 35-mm fields of view and the 10-mm depths of field of the three cameras. While the cameras have a pixel size of 9 μm
by 9 μm, the system is only triggered when particles with a maximum dimension of greater than 0.1 mm are detected by the
near-infrared sensors.

Although the MASC processing algorithm was originally written in MATLAB, a version written in Python also exists and
it is this version of the ellipse fitting method that will be analyzed here (Shkurko et al., 2016). To simplify matching particles
between the three cameras, MASC only processes images that contain a single precipitation particle and, of these, only particles
that are in focus are actually analyzed. The method used to determine whether a particle is in focus is detailed in Garrett et al.
(2012). Similar to PIP, MASC also fits an ellipse to the precipitation particles to determine the particle shape properties. In
the Python version of the MASC algorithm, this is accomplished using the fitEllipse function within the OpenCV package
(https://docs.opencv.org/3.4/, accessed 15 December 2021), which uses the 'LIN' algebraic distance ellipse-fitting algorithm
described in (Fitzgibbon and Fisher, 1995) and returns both the major and minor axis lengths as well as the orientation angle
of the fitted ellipse.

3.3 Two-Dimensional Video Disdrometer (2DVD)

2DVD (Kruger and Krajewski, 2002; Schönhuber et al., 2007) uses two orthogonally oriented line-scan cameras to take mea-
surements of backlit precipitation particles. These horizontally scanning line-scan cameras capture a series of one-dimensional
images of the particle as it passes through the viewing plane. Each camera captures a one dimensional image every 18μs and
these one-dimensional images are then pieced together to produce a two-dimensional image of the precipitation particle for
each camera. Furthermore, since the viewing planes of the two cameras are separated by 6–7 mm, the particle fall speed can
be measured via the difference in the arrival time of the particle in each viewing plane. Although 2DVD was designed to study
rain drops, the instrument has been used to study snow as well (e.g., Huang et al., 2010).

Because the 2DVD cameras do not capture the entire shape of the particle at once, consideration must be given for how the
horizontal motion impacts the perceived particle shape. For a particle with no horizontal motion, the result of piecing together
the one-dimensional images will result in a particle image that depicts a close approximation of the actual particle. If the
particle is moving horizontally, however, then the particle will appear to have been shifted horizontally in each subsequent one-
dimensional image. The end result of imaging a horizontally moving particle is that the particle will appear to have undergone
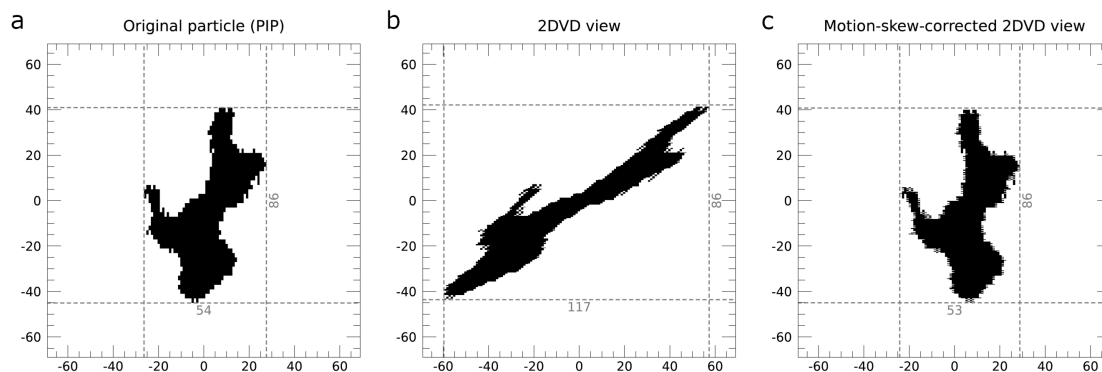
Figure 1. An example of the emulated 2DVD measurements and our unskewing algorithm including (a) the original particle as captured by the PIP camera, (b) the emulated 2DVD view of the particle before the skew correction, and (c) the emulated 2DVD view of the particle after applying our skew correction. The coordinates are in units of PIP pixels from the particle center. The gray dashed lines indicate the extent of the bounding boxes for each view of the particle, with the length of each bounding box edge marked on the bottom and right edges in units of PIP pixels.

a shear transformation relative to the actual particle. Figure 1a–b depicts an example of this shearing effect by sampling a PIP image as though a 2DVD instrument were measuring the particle (see section 4.2).

The image skewing produced by the horizontal movement of particles, as evident in Fig. 1b, can invalidate certain 2DVD measurements. While an algorithm designed to remove these effects exists, the algorithm is, unfortunately, in the form of a

155 proprietary software package and, as such, its exact inner workings are unclear. That said, Kruger and Krajewski (2002) state that the algorithm works by assuming the top-most and bottom-most pixels of the particle should be vertically aligned with one another. The algorithm then skews the image in the opposite direction to a sufficient degree to place the top- and bottom-most pixels into vertical alignment. An approximation of the unskewing algorithm has been applied to the particle in Fig. 1c; this approximation of the unskewing algorithm is described in section 4.2.

160 Unlike MASC and PIP, the equivalent diameter that is actually recorded in the 2DVD data sets is an equi-volume diameter. The details of how this equi-volume diameter is computed from the raw 2DVD data can be found in Schönhuber et al. (2008). Briefly, the calculation works by assuming the shape observed in each pair of scan lines, captured by the orthogonal pair of line-scan cameras, is that of an elliptical cylinder whose major and minor axes are entirely captured by the pair of line-scan cameras. The volumes of these elliptical cylinders are then summed to determine the total volume of the particle. While this

165 method is reasonable for approximately ellipsoidal particles (e.g., raindrops or hailstones), the complex surface structures present in snowflakes and snowflake aggregates can invalidate the volume calculations.

4 Method

The ideal method for comparing the measurements made of snowflakes by each of these three instruments would be to have all three instruments measure the same particles simultaneously. Due to the construction of each of these instruments, however,
170 this is not physically possible. Instead, the algorithms used by each instrument to determine particle shape will be analyzed by emulating each instrument's analysis algorithms using PIP-recorded images as an input. PIP images are used as the basis of the measurement emulation rather than MASC images because the PIP captures considerably more particles in its sampling volume than does MASC.

The PIP images used for this study come in the form of Audio Video Interleave (AVI) video files. PIP produces these video
175 files every 10 minutes and each video file contains the first 2000 frames in which PIP identified a particle during that 10 minute period. If fewer than 2000 frames contained particles during a given 10 minute period, the video file will contain fewer than 2000 frames. A description of how we emulate the MASC and 2DVD observations is provided in sections 4.1 and 4.2 and an overview of the method by which we process the PIP AVI video files in order to apply our emulated algorithms is presented in Appendix B. Additionally, we will test and evaluate an alternative ellipse-fitting method, hereafter referred to as the tensor
180 method, for retrieving particle length and width from the PIP images; this method is described in section 4.3.

For the emulation of both MASC and 2DVD as well as the tensor ellipse-fitting method, the particle image pixels have values of either zero (non-particle pixel) or one (particle pixel). Any pixel that does not have the background value (i.e., white) is included as part of the particle. Particles in the AVI files are matched to the PIP measurements by using a region grow approach, whereby a coherent region is grown from a single point by checking its eight neighboring pixels for inclusion in
185 the region and then repeating the process with each newly included pixel. The region grow approach is initially attempted at the PIP-determined particle centroid. For some particles with either large concave regions or holes, the PIP-measured particle center can correspond to a non-particle pixel. In these instances, an attempt is made to locate a new starting pixel for the region grow technique by searching the following (x,y) coordinate offsets in the given order: (-1,0), (1,0), (0,-1), (-1,-1), (1,-1), (0,1), (-1,1), (1,1). If a particle pixel is not located at any of these center offset positions, the process is repeated after multiplying
190 the offsets by a factor of two; in cases where a particle pixel remains elusive, the process is repeated with multiples of three and then four. If no particle pixels are located after checking these 32 offset positions, the particle is considered invalid and is ignored. Additionally, only particles that appear both in the particle tables (i.e., the PIP files ending in '_a_p.dat') and in one of the two velocity tables (i.e., the PIP files ending in either '_a_v_1.dat' or '_a_v_2.dat') are considered here as the variables contained in these files are necessary for performing the emulations.

195 ### 4.1 MASC emulation

Our emulation of the MASC processing algorithm is based on the algorithm used for the U.S. Department of Energy Atmospheric Radiation Measurement (ARM) program MASC instruments (Stuefer and Bailey, 2016; Shkurko et al., 2016). Because both the PIP and MASC ultimately make their measurements using two-dimensional images, no special processing is performed to prepare the images before the emulated MASC measurements are made. The emulation of the actual mea-

surements will be performed by using the same ellipse fitting function as is used by the ARM MASC instrument algorithm,
specifically the fitEllipse function from the OpenCV Python package (see section 3.2). Although the MASC cameras have a
considerably higher resolution than the PIP camera, it is worth noting that the effects of the camera resolution difference are
expected to be negligible in terms of shape fitting. One exception to this is that the fitEllipse function effectively requires at
least five pixels within the target particle; for the actual MASC measurements, this represents a particle far smaller than the
threshold minimum measured size of 0.1 mm. In the case of the emulated MASC, a five pixel particle would have an area of
0.5 mm^2 and a maximum dimension of at least 0.3 mm as the PIP pixels are calibrated to be 0.1 mm of each side. To avoid
having particles that can only be analyzed by a subset of the measurement algorithms, our comparisons here will only consider
particles which have an equivalent area of at least 0.5 mm^2.

4.2 2DVD emulation

The 2DVD instrument captures a series of one-dimensional images as a particle falls through the observing volume. As such,
the PIP images must be resampled in a way that mimics the 2DVD instrument itself. To this end, we use snapshots of the
PIP-observed particles and replicate the horizontal and vertical motions of the particles, as measured by PIP, using bilinear
interpolation. The vertical motion is replicated by shifting the vertical coordinates of the bilinear interpolation upward by an
amount equal to the product of the particle fall speed and the camera observation frequency; for 2DVD, the camera observation
frequency is 68200 Hz. The horizontal motion is replicated by shifting the particle snapshot pixel locations horizontally in the
direction of particle motion by an amount equal to the distance traveled by the particle during the elapsed time of the emulated
observations, to the nearest 0.1 mm. This elapsed time is equal to the product of the inverse of the camera observation frequency
and the number of times the particle has been sampled in the vertical up until that point (i.e., the number of emulated 2DVD
line scans performed). When performing the interpolations, only the interpolated pixels with a value of one are considered part
of the emulated 2DVD observation.

An example of an emulated 2DVD observation is depicted in Fig. 1 with the original, PIP-observed, particle image depicted
in Fig. 1a and the emulated 2DVD particle image depicted in Fig. 1b. Note the considerable skewing that has occurred in
the emulated 2DVD image relative to the PIP image due to the horizontal movement of the particle towards the left as it
passed through the virtual line scan camera. As previously mentioned, 2DVD applies an unskewing algorithm to correct for the
distortions introduced by the horizontal motion of the particle. Because this algorithm is part of a proprietary software package
and not openly available, we have chosen to approximate the effects of the algorithm based on the conceptual description
provided by Kruger and Krajewski (2002).

Recall, from section 3.3, that the 2DVD unskewing algorithm works by assuming that the top-most and bottom-most points
on an observed particle are actually vertically aligned with one another (Kruger and Krajewski, 2002). In the event of multiple
particle pixels appearing on the top-most or bottom-most scan line, it is unclear how the actual algorithm selects the top-most
or bottom-most point of the particle. To this end, we have decided to define the top-most and bottom-most points of the particle
as the mean horizontal location of the particle pixels on the top-most and bottom-most scan lines, respectively.

The actual unskewing process in our algorithm works by linearly interpolating the horizontal offset, as implied by the motion-skewed locations of the top-most and bottom-most points of the particle, to the vertical position of each scan line. Each

235 scan line is then horizontally shifted by the appropriate offset via another linear interpolation. The value of the interpolated pixels are then rounded to either zero, indicating a non-particle pixel, or one, indicating a particle pixel. Figure 1c depicts the result of applying the unskewing algorithm; note the slight differences in the apparent particle orientation between the original image (Fig. 1a) and the unskewed image (Fig. 1c). We will examine the effects of these differences on the accuracy of the 2DVD bounding-box measurements in section 5.3.

240 ### 4.3 Tensor-fitted ellipse

To provide an additional point of comparison for the particle measurements, we also implemented an alternative ellipse fitting strategy, referred to here as the tensor method, that uses the method implemented in the fit_ellipse program in the Coyote IDL Library (accessible at http://www.idlcoyote.com, accessed 15 December 2021). This method works by computing the eigenvalues, e_1 and e_2, of a mass distribution tensor, which is defined as

245
$$\tau = \begin{bmatrix} \overline{(\Delta y)^2} & \overline{\Delta x \Delta y} \\ \overline{\Delta x \Delta y} & \overline{(\Delta y)^2} \end{bmatrix},$$
(1)

where Δx and Δy are the distances from the particle centroid in the horizontal and vertical directions, respectively. The semimajor and semiminor axes, a and b, respectively, are then calculated from the eingenvalues via

$$a = 2\sqrt{e_1} \quad \text{and} \quad b = 2\sqrt{e_2}.$$
(2)

The major and minor axes of the fitted ellipse can then be obtained simply by doubling the semimajor and semiminor axes.

250 Finally, in the interest of completeness, the tensor-fitted ellipse orientation, measured counterclockwise from the positive x axis, is computed as $\arctan(e_2/e_1) - 90°$. As will be discussed in section 5.2, the tensor-fitted ellipse method produces similar, although not identical, fits to that of the emulated MASC method.

5 Results

5.1 Area and equivalent diameter

255 There are a number of factors of varying importance that can affect the measurement of the particle area and, therefore, the equivalent diameter. For this study, however, we will examine the theoretical accuracy and precision of the MASC, PIP, and 2DVD area and equivalent diameter measurements in terms of motion blur as determined from the pixel resolution, exposure time (i.e., shutter speed), and particle fall speed. For both PIP and MASC, the equivalent diameter is determined from the area of the two-dimensional projection of the particle, which is measured by counting the number of pixels within the particle and

260 then multiplying that number by the calibrated pixel size (i.e., the area each pixel represents in the image). As discussed in section 3.3, 2DVD, however, reports an equi-volume diameter rather than an equi-area diameter by summing the values of

stacked elliptical cylinders. For simplicity, we will only consider the effects of motion blur on the two-dimensional area and equi-area diameter from a single camera for 2DVD rather than the estimated volume and equi-volume diameter that the 2DVD software computes. It should be noted that there are a number of factors that are not being considered in the present study.

265 For simplicity, we have not included the effects of image thresholding on the area measurements nor have we considered the effects of each camera's point spread function, which describes how light is distributed amongst each of the imaging pixels of the camera sensor. We also do not consider the effects of the circle of confusion (i.e., the blurring of out-of-focus particles) as this will only be an issue if the particle is located outside of the instrument's depth of field.

The MASC setup used during ICE-POP had a pixel resolution of 33.5 μm and an exposure time of 40 μs or 1/25000th of a

270 second (Jacopo Grazioli, 2021, personal communication). With this exposure time, a single point on an arbitrary precipitation particle falling directly downwards at 1 m s^{-1} would appear as a 40 μm long vertical line. With a pixel resolution of 33.5 μm, there would be minor motion blurring as a single point on the particle would contribute to at least two pixels and possibly three, although in the three pixel case the contribution to two of the pixels would be very minor. This blurring would effectively add an extra pixel below all of the lower-edge pixels and above all the upper-edge pixels of a particle, thereby increasing the area

275 and, therefore, the equivalent diameter. For a 4 m s^{-1} fall speed, which would be an extremely fast fall speed for a snowflake, the point would appear as a 160 μm line, appearing in at least five pixels in the ICE-POP MASC.

PIP has an exposure time of 28 μs or ∼1/35700th of a second. With this exposure time, a single point on a precipitation particle falling vertically at 1 m s^{-1} would appear as a 28 μm long vertical line; however, because PIP has a pixel size of 0.1 mm (100 μm), the motion blurring would be almost negligible. In the case of a particle falling at 4 m s^{-1}, the single point would

280 produce a 112 μm long line for the given exposure time and, as such, would contribute to at least two pixels. Complicating this, however, is that PIP compresses the images prior to transmission. As part of the PIP compression algorithm, pairs of vertically adjacent pixels are averaged together, resulting in a pixel size of 0.1 mm by 0.2 mm while the image is compressed. When the image is decompressed, this averaged value is assigned to the individual pixels making up the pixel pair (L. Bliven, 2021, personal communication), producing an effective resolution of 0.1 mm by 0.2 mm. Because the motion blurring effects apply

285 to the pre-compression pixels rather than the post-compression pixels, the interaction between image compression and motion blurring warrants a closer examination.

Figure 2 depicts schematic representations of how the effects of motion blurring and image compression interact for a single column of PIP pixels when viewing a 0.4-mm tall particle. Note, for the purposes of this demonstration, we have arbitrarily decided that a pixel will count as being part of the particle when it appears to be at least 50% covered by the particle, taking

290 both motion blurring and compression into account. In actuality, the assignment of a pixel to a particle is more complicated and is described in Newman et al. (2009). The simplest example is that of a particle suspended in air (i.e., with zero fall speed), which will experience no motion blurring (Fig. 2a). The left column of pixels depicts the pre-compression view, which sees the particle as being four pixels tall (i.e., 0.4 mm) as there is no motion blurring or compression. Because a particle can be located anywhere relative to the compression algorithm's vertically paired pixels, we must examine the two extreme possible

295 alignments to understand the range of possible effects. In the first of these possibilities, the top edge of the particle is aligned with the top of the upper pixel in the pixel pair, depicted in the center column of pixels. This alignment results in the post-
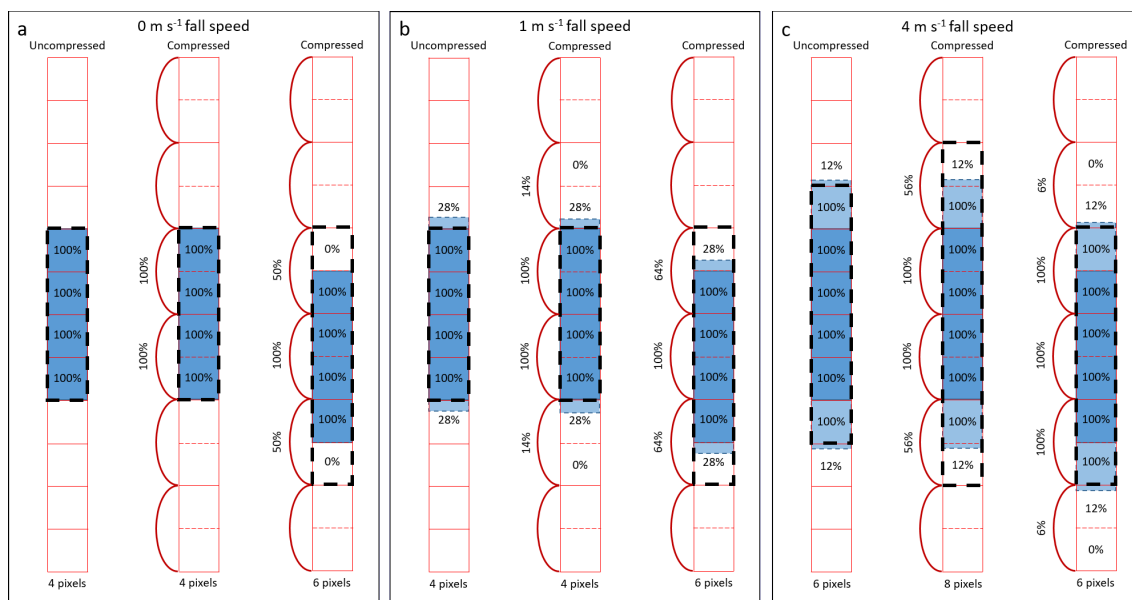
Figure 2. Schematic depictions of the combined effects of PIP image compression and motion blurring for a 0.4 mm tall particle (a) suspended in air, (b) falling at 1 m s^{-1}, and (c) falling at 4 m s^{-1}. The red boxes indicate individual PIP pixels and the dark red braces indicate the pairs of pixels that are averaged together during the image compression. The darker blue shading indicates the area covered by the actual particle and the lighter blue shading indicates the additional area that appears to be covered by the particle due to motion blurring. The dashed black box indicates the pixels which appear to be contained within the particle, taking into account both motion blur and compression; for demonstration purposes, we count a pixel as being in the particle if it appears to be at least 50% covered after motion blur and compression effects are applied. The value listed inside each pixel indicates the percent coverage of that pixel by the apparent particle prior to compression and the value listed along each brace indicates the percent coverage of the paired pixels post-compression (this value is assigned to both of the paired pixels when the image is decompressed for analysis). In each panel, the left column of pixels represents the view before compression and the right two columns of pixels represent the view after compress, corresponding to the two extremes of how a particle could align to the compression pixel pairs.

compression image also depicting a particle that is four pixels tall. In the second of these possibilities, the top edge of the particle is aligned with the top of the lower pixel in the pixel pair, depicted in the right column of pixels. This alignment results in the post-compression image depicting the particle as being six pixels tall instead of four pixels tall because the completely

300   covered top- and bottom-most pixels of the particle are averaged with completely uncovered non-particle pixels resulting in a post-compression pair of pixels that each appear to be 50% covered by the particle (as indicated by the number next to the dark red brace in Fig. 2a). As such, the image compression can add between zero and two additional pixels to the height of a suspended particle.

      For a PIP-viewed particle with a non-zero fall speed, both both motion blurring and image compression must be taken into

305   account; schematic representations for particles falling a 1 m s^{-1} and 4 m s^{-1} are depicted in Fig. 2b and Fig. 2c, respectively.

Because of our prescribed threshold of 50% coverage, the 1-m-s^{-1} fall speed case ends up producing the same result as the suspended particle case: the addition of between zero and two additional pixels to the height. For a particle falling at 4 m s^{-1}, however, the motion blurring adds an extra two pixels to the height prior to compression and the image compression adds an additional zero to two pixels; in total, the motion blurring and compression effects add between two and four pixels to the
310   height of the particle.

Of the three instruments considered in this study, 2DVD has the shortest exposure time at 18μs or ~1/55500th of a second (Schönhuber et al., 2008). Each 2DVD line-scan camera has 512 photodetectors that are calibrated to observe a 100-mm wide field of view (Kruger and Krajewski, 2002), from which we can infer that the pixel size is ~0.195 mm. With the shortest exposure time and largest pixel size, it is unsurprising that 2DVD should be the most resilient to motion blur effects according
315   to our analysis of the camera setups. Even for a snowflake with an extremely fast fall speed of 4 m s^{-1}, a single point on the snowflake would only move 72 μm during the exposure time, which is only ~37% of the pixel size assuming the camera elements gather light isotropically in the vertical and horizontal directions.

The extent to which the motion blurring discussed above might impact the measurement of particle area and, by extension, the equivalent diameter, is highly dependent on the shape and orientation of the particle. The area errors introduced by motion
320   blur will increase as the number of particle pixels with an adjacent non-particle pixel either above or below increases; these particle pixels are hereafter referred to as top-edge or bottom-edge pixels, respectively. Motion blur of the top-edge pixels occurs when the particle leaves those pixels during the image exposure period while motion blur for the bottom-edge pixels occurs when the particle enters those pixels during the image exposure period. The motion blur effects will impact the area calculation at both the top-edge pixels and bottom-edge pixels simultaneously. For a particle with an entirely convex edge,
325   the total number of top- and bottom-edge pixels will be equal to twice the horizontal width of the particle, in pixels; for non-convex particles, the combined number of top- and bottom-edge pixels will depend on how many additional top- and bottom-edge pixels, if any, the concave edge regions add to the particle.

Figure 3 depicts the impacts of motion blurring on the area and equivalent diameter measurements for a perfectly circular particle being observed by MASC and PIP; 2DVD is not included in this figure as the motion blurring effects are negligible
330   by comparison. Note that the PIP values also account for the effects of the image compression algorithm, using the average number of additional pixels for each fall speed. While the relative impact of the area and equivalent diameter errors introduced by motion blur depend on the application for which the measurements are being used, we can draw a number of general conclusions from our analysis. Key among these is that very small particles will experience considerably greater impact from the motion blur errors than will larger particles falling at the same rate; this is particularly evident in the fractional bias plots
335   (Fig. 3c,d). Generally speaking, however, smaller particles of a given ice crystal habit will tend to have a slower fall speed than larger particles of that same habit and will, therefore, typically experience less motion blur. Even with a very fast fall speed of 4 m s^{-1}, the overestimation of the equivalent diameter for very large circular particles (diameter $\gtrsim$ 10 mm) is approximately two orders of magnitude or more smaller than the actual equivalent diameter. Critical to interpreting and applying these results is the fact that we assumed that the particles are perfectly circular. As the the horizontal dimension of the particle grows relative to
340   the vertical dimension, the relative (and absolute) effects of motion blurring on the area and equivalent diameter measurements

will also grow. Additionally, as the particle outline becomes more complex and the number of top- and bottom-edge pixels in the particle increases, the measurement errors due to motion blur will also increase.

The differences between PIP, MASC, and 2DVD measurements of area and equi-area diameter are best considered in terms of precision and accuracy. As demonstrated in Fig. 3, PIP will produce a slightly less accurate measurement of area and

345 equivalent diameter than MASC in the presence of motion blurring. Interestingly, were the PIP images not compressed prior to their analysis, the PIP would produce slight more accurate measurements than MASC (not shown). That said, MASC will produce a considerably more precise measurement than either PIP or 2DVD due to the very high resolution of the MASC cameras relative to the other cameras examined in this study. As we established above, the 2DVD should be the least effected by motion blur and, as a result, should have the most accurate area measurements. Due to the complicating factor of the PIP

350 image compression algorithm, it is unclear whether the precision of the PIP, which has 0.1 mm tall camera pixels but 0.2 mm tall effective pixels, would have greater or approximately equal precision as 2DVD, which has ∼0.195 mm pixels, as this would likely depend on the alignment between the particle edges and the vertically paired pixels used in the PIP image compression algorithm. For a worst-case scenario, however, the precision of the PIP would likely be similar to that of the 2DVD as the post-compression effective PIP pixel height is only slightly greater than that of the 2DVD.

355 **5.2   MASC and PIP shape-fitting measurements**

As discussed in section 4, the PIP data for the period between 0000 UTC 7 March and 0000 UTC 9 March 2018 at the ICE-POP MHS observation site was processed using algorithms designed to emulate both the MASC and 2DVD measurements of particle dimension. The present section will focus on the shape-fitting techniques of MASC and PIP as well as an alternative ellipse-fitting technique, referred to here as the tensor method. A comparison of the bounding box measurement techniques

360 used by PIP and 2DVD will be the subject of a separate section (section 5.3) rather than being included here. Although the tensor-fitted ellipse measurements will be used here as a point of comparison between the various instrument algorithms, it should be noted that the tensor-fitted ellipse measurements are not a 'ground truth' and are subject to errors of their own.

Comparing the PIP-fitted ellipse particle dimensions to those of the tensor-fitted ellipse, we found that the PIP-fitted ellipse tends to overestimate the long dimension of the particle (Fig. 4a), measured as the major axis of the fitted ellipse, and under-

365 estimate the short dimension (Fig. 4d), measured as the minor axis of the fitted ellipse, relative to the tensor-fitted ellipse. As a result, the aspect ratio, computed as the short dimension divided by the long dimension, is almost always underestimated by the PIP-fitted ellipse relative to the tensor-fitted ellipse. This underestimation is particularly noticeable for larger tensor-fitted ellipse aspect ratios with the PIP-fitted ellipse aspect ratio rarely exceeding 0.6 and never reaching 0.7 during this event, despite there being a period of lump graupel, which should have a relatively high aspect ratio due to its almost spherical shape, on 8

370 March (Fig. 5a).

Using the aspect ratio computed from the PIP-fitted rectangle instead of the PIP-fitted ellipse appears to increase the spread in both long and short dimensions, producing more agreement with the tensor-fitted ellipse measurements (Fig. 4b,e). As a result, the PIP-fitted rectangle aspect ratio does not suffer from the artificial cap that was present with the PIP-fitted ellipse aspect ratio (Fig. 4h). That said, the PIP-fitted rectangle aspect ratio still has a tendency to greatly underestimate the aspect
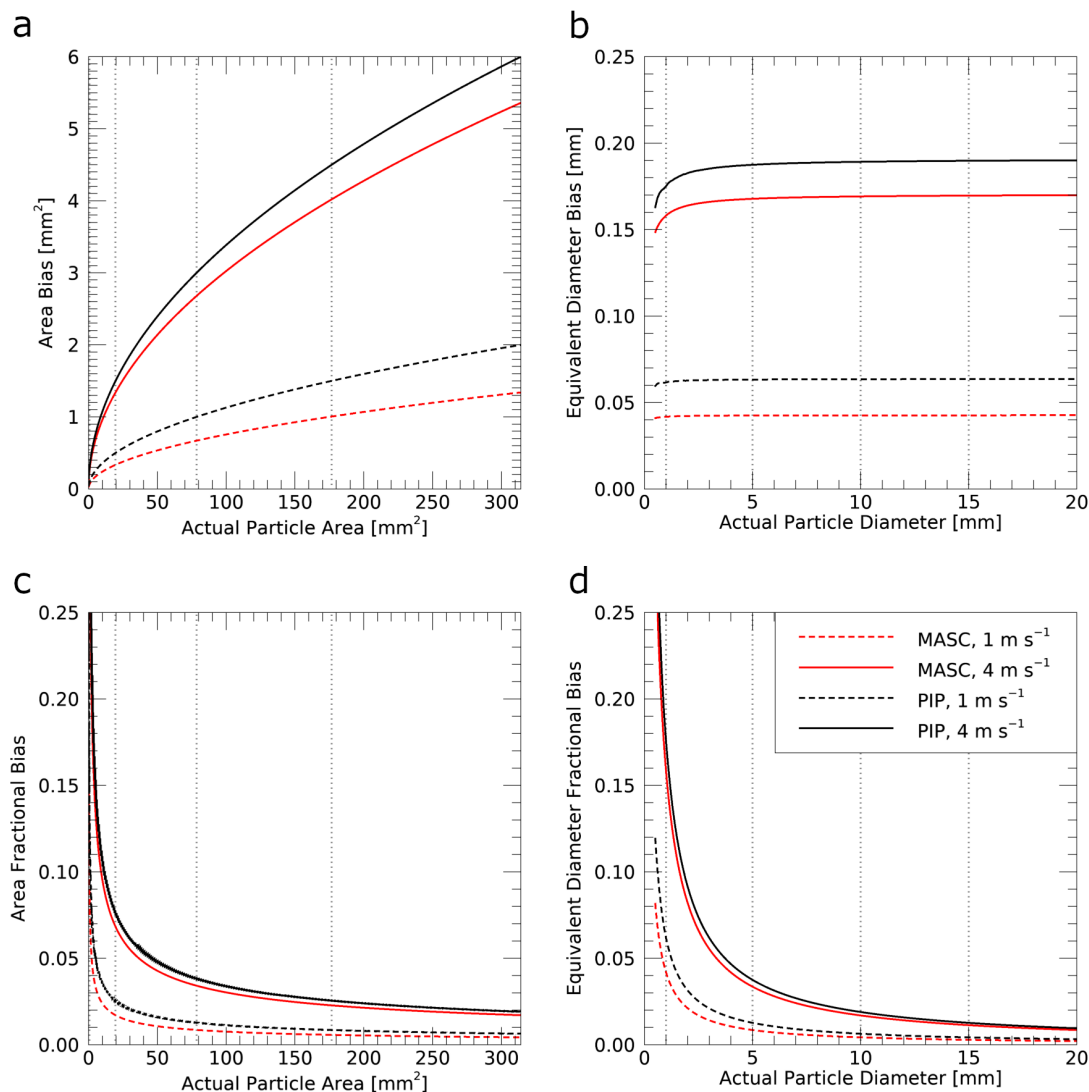
Figure 3. Approximate effects of motion blur on (a,c) measured area [mm^2] and (b,d) measured equivalent diameter [mm] for hypothetical perfectly circular particles falling at (dashed line) 1 m s^{-1} and (solid line) 4 m s^{-1} as (red) MASC and (black) PIP would measure them. The effects are portrayed both in terms of (a,b) the bias, computed as the difference between the motion-blurred quantity and the actual particle quantity, as well as (c,d) the fractional bias, computed as the bias divided by the actual particle quantity. Calculations are performed based on the number of additional full pixels added by motion blur to a circular particle. Specifically, for each additional pixel of diameter, the motion blur will add two (eight) pixels to the MASC measurement of a particle falling at 1 m s^{-1} (4 m s^{-1}) and one (three) pixels to the PIP measurement of a particle falling at 1 m s^{-1} (4 m s^{-1}). Gray vertical lines indicate the corresponding quantity for particles with actual diameters of 1, 5, 10, and 15 mm.
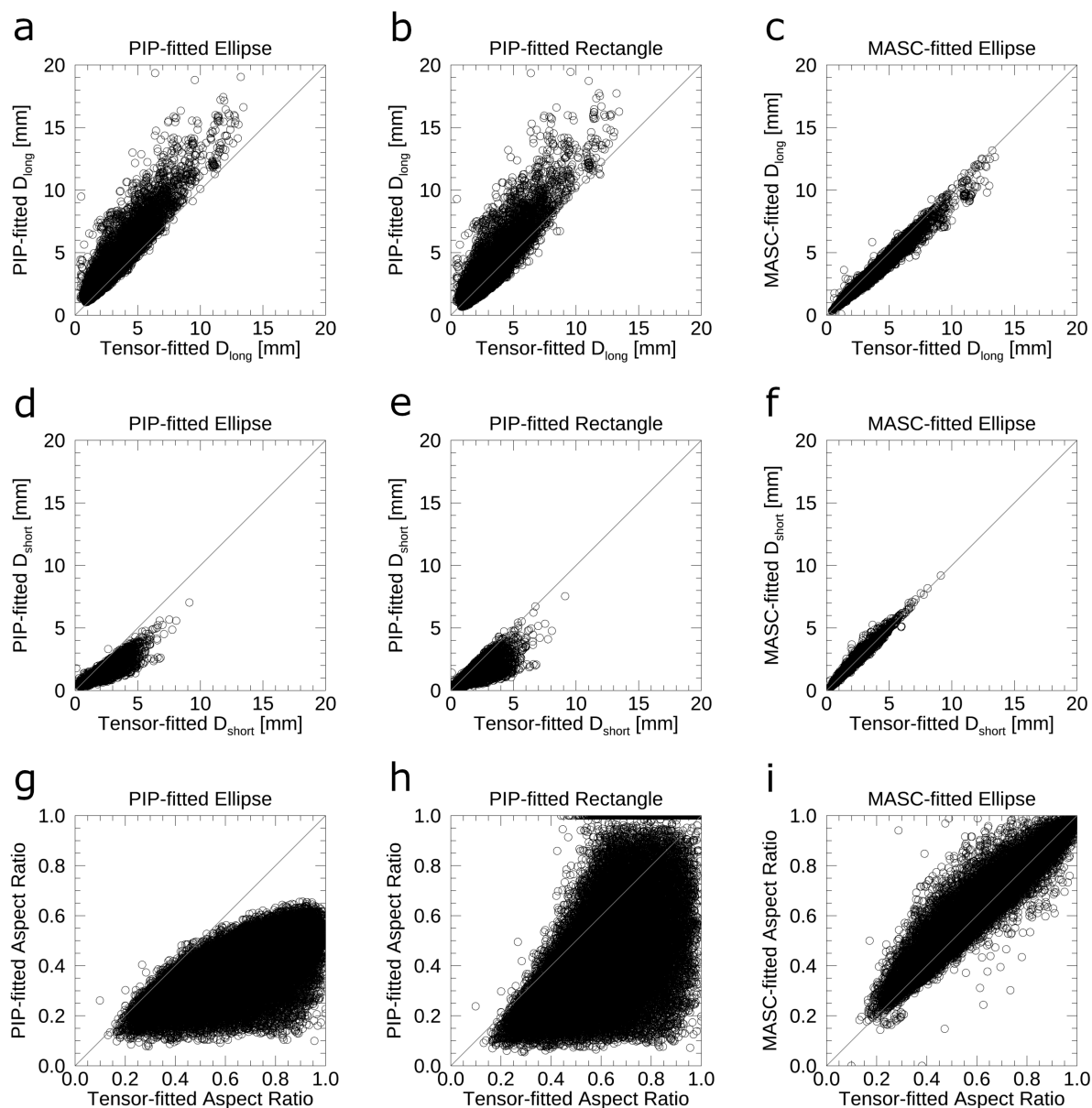
Figure 4. Scatterplots of (a-c) particle long dimension in mm, (d-f) particle short dimension in mm, and (g-i) particle aspect ratio for (a,d,g) the PIP-fitted ellipse, (b,e,h) the PIP-fitted rectangle, and (c,f,i) the emulated MASC-fitted ellipse as a function of the tensor-fitted ellipse values. Data points are indicated by open circles and only data for particles with a PIP-measured area greater than 0.5 mm^2 are included. PIP data was collected between 0000 UTC March 2018 and 0000 UTC 9 March 2018 at the ICE-POP MHS site.

375 ratio relative to the tensor-fitted ellipse aspect ratio (Fig. 5b). Interestingly, the PIP-fitted rectangular aspect ratio frequently has a value of one but very rarely has a value between 0.9 and one; this peculiarity will be revisited later in this section. It
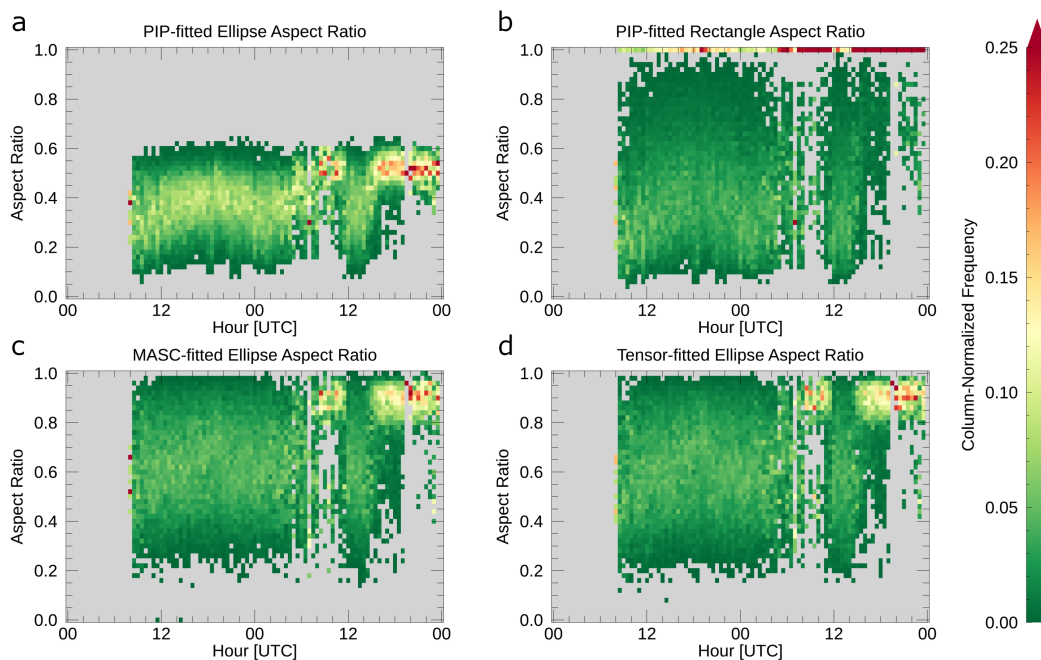
Figure 5. Time series of the (a) PIP-fitted ellipse and (b) PIP-fitted rectangle, (c) emulated MASC-fitted ellipse, and (d) tensor-fitted ellipse aspect ratio distributions for the 7–8 March 2018 case. Only particles with an area of at least 0.5 mm^2 were included in the histograms. The bin counts of each column have been normalized such that they add up to one.

should be noted, however, that the PIP-fitted rectangle aspect ratios do capture the expected increase in aspect ratio that would be expected during the period of lump graupel precipitation on 8 March.

In contrast to the two sets of PIP-fitted measurements, the MASC-fitted ellipse measurements show very good agreement
380 with the tensor-fitted ellipse measurements of both the long and short dimension of the fitted particles (Fig. 4c,f). As a result, the aspect ratios computed from the MASC-fitted and tensor-fitted ellipses are in fairly good agreement as well (Fig. 4i). This general agreement between the particle dimensions measured from the MASC-fitted and tensor-fitted ellipses suggests that these two shape fitting algorithms may be giving more reliable results than the PIP-fitted ellipse or rectangle algorithms. To gain insight into whether the MASC- and tensor-fitted ellipse algorithms are, in fact, performing better than the PIP algorithms,
385 we will take a closer look at individual particles.

Figure 6a-d depicts snapshots of particles taken from the PIP AVI files with the fitted shapes from the various fitting algorithms depicted in Fig. 6e-h. For simplicity, these particles will be referred to by the Fig. 6 panel letter of the unannotated panels (i.e. panels a–d). Particles (a) and (b) are both likely some type of aggregate frozen precipitation based on their odd shapes. Based on the relatively circular shapes of the remaining two particles, relatively high fall speeds, and lack of a warm
390 nose in a nearby thermodynamic sounding (not shown), particles (c) and (d) are likely both examples of lump graupel. Qualitative and quantitative inspection of the particles in Fig. 6 and Table 1 supports the patterns identified by the scatter-plot
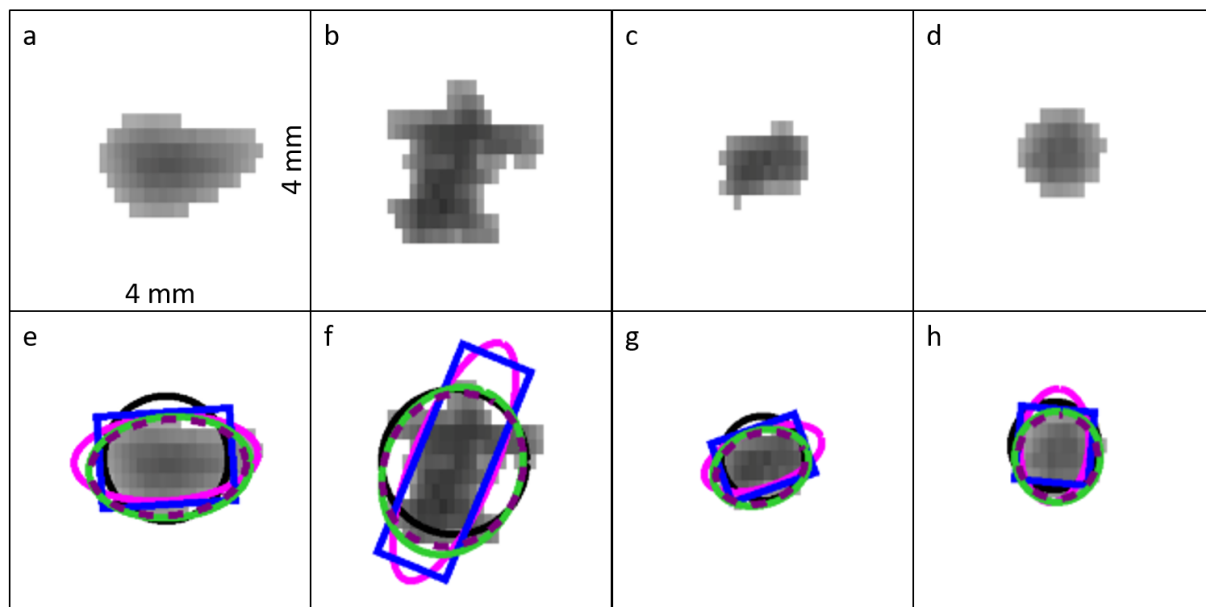
Figure 6. Snapshots of three particles as viewed by PIP collected by PIP at approximately (a,b,e,f) 1904 UTC 7 March 2018 and (c,d,g,h) 1756 UTC 8 March 2018 with (e-h) overlaid particle shape estimates as determined by the (black) area-equivalent circle, (magenta) PIP-fitted ellipse, (blue) PIP-fitted rectangle, (purple dashed) emulated MASC-fitted ellipse, and (green) tensor-fitted ellipse. Each panel represents a square that is 4-mm long on each side. The dimensions of the fitted shapes for each particle are presented in Table 1.

analysis performed above. Specifically, the PIP-fitted ellipse appears to always overestimate the particle long dimension; the PIP-fitted rectangle appears to sometimes overestimate, sometimes underestimate, and sometimes accurately capture the particle long dimension; and, finally, the emulated MASC-fitted and the tensor-fitted ellipses tend to produce fairly similar particle

395 dimensions. Additionally, visual examination of these and other (not shown) individual particles suggests that the emulated MASC-fitted and the tensor-fitted ellipses tend to provide more reasonable estimates of particle dimension than either of the PIP-fitted shapes.

The primary cause of the discrepancies between the actual particle shape and the PIP-fitted ellipse major and minor axes is rooted in the reliance on only the particle area and perimeter for making the PIP fits, as discussed in section 3.1. For particles

400 with complicated outlines, such as particle (b), the perimeter of the particle is far greater than the perimeter would be for an ellipse or rectangle of equal length and width or of equal area. To make up for the extra perimeter for a given area, the PIP-fitted ellipse or rectangle must have a larger long dimension at the expense of the short dimension; note, extending the short dimension at the expense of the long dimension would result in a smaller perimeter for a given area.

The relationship between excess perimeter for a given area, relative to a perfect ellipsoid, and error in the PIP-fitted ellipse

405 or rectangle dimension lengths is demonstrated in Fig. 7 for a hypothetical particle that we will treat as being generally circular with an edge that undulates about a radius of 0.5 mm. The amplitude of this undulation is represented in Fig. 7 by the perimeter stretching factor, computed as the actual perimeter of a particle divided by the perimeter of a circle of equal area to the particle.

Table 1. Dimensions and aspect ratios of the fitted shapes for various particle fits depicted in Fig. 6, referenced by the figure panel letter for the unannotated particle images. The perimeter stretching factor is computed by dividing the actual particle perimeter by the perimeter of a circle of equal area to the particle.

| | Fig. 6 panel | | | |
Fitted-shape measurement	(a)	(b)	(c)	(d)
Equivalent diameter [mm]	1.680	1.950	1.130	1.180
Perimeter stretching factor	1.148	1.308	1.144	1.068
PIP-fitted ellipse				
Major-axis length [mm]	2.478	3.434	1.660	1.529
Minor-axis length [mm]	1.141	1.105	0.767	0.916
Aspect ratio	0.460	0.322	0.462	0.599
PIP-fitted rectangle				
Long-side length [mm]	1.790	3.020	1.190	0.990
Short-axis length [mm]	1.240	0.990	0.840	0.990
Aspect ratio	0.693	0.328	0.706	1.000
Emulated MASC-fitted ellipse				
Major-axis length [mm]	2.093	2.121	1.238	1.132
Minor-axis length [mm]	1.288	1.831	0.926	1.065
Aspect ratio	0.615	0.863	0.748	0.941
Tensor-fitted ellipse				
Major-axis length [mm]	2.178	2.311	1.331	1.227
Minor-axis length [mm]	1.363	1.831	0.990	1.150
Aspect ratio	0.626	0.792	0.744	0.938

For our hypothetical particle, the perimeter stretching factor is prescribed and the actual perimeter is computed by multiplying the perimeter of a 0.5-mm-radius circle by the perimeter stretching factor. A perimeter stretching factor of one will result in a

410 perfect circle while larger perimeter stretching factors would be associated with particles with increasingly rough edges. For clarity, we do not construct a particle with undulating edges to make the measurements, but instead merely parameterize its existence using the perimeter stretching factor. As the PIP-fitting method only requires perimeter and area, our parameterization of the hypothetical particle is sufficient to perform an ellipse or rectangle fit without constructing the hypothetical particle itself. The equations used to make the PIP fits are derived in appendix A. Note that nothing in these equations relates to the actual

415 shape of the particle itself (e.g., circular or elliptical); this missing information is, in fact, the core issue with both the PIP ellipse and rectangle fits. Without knowledge of the underlying distribution of pixels within the particle, the PIP algorithm assumes all particles are either smooth-edged ellipses or rectangles, depending on which fit is used.
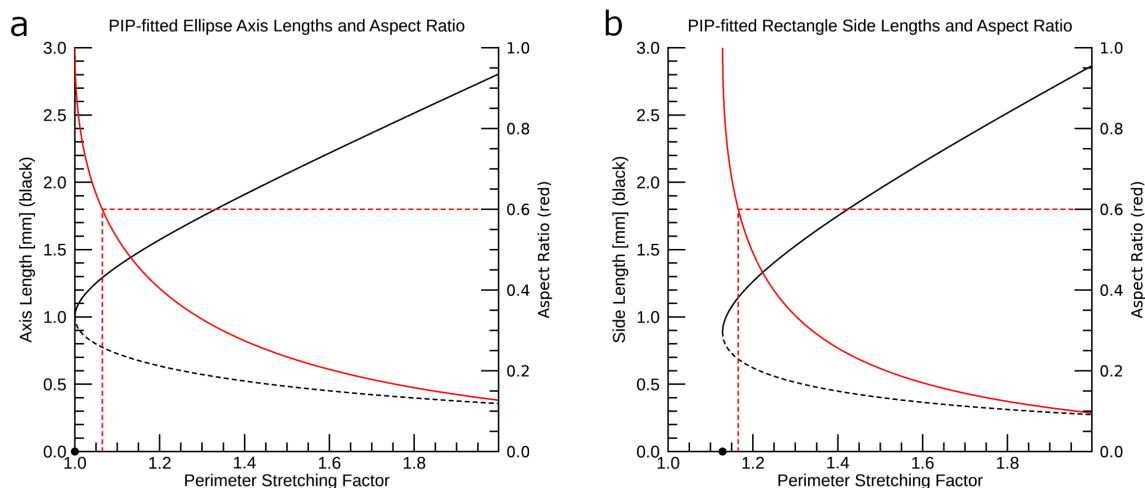
Figure 7. Demonstration of the impact of excess perimeter for a given area on the (a) PIP-fitted ellipse and (b) PIP-fitted rectangle long-axis length (black solid), short-axis length (black dashed), and aspect ratio (red solid). This example uses a circle with a radius of 0.5 mm to compute the base perimeter and area. The perimeter of this circle is then multiplied by the perimeter stretching factor before the ellipse or rectangle fitting is performed according to the method used by PIP. The red dashed lines highlight the perimeter stretching factor that corresponds to an aspect ratio of 0.6 and the black dot indicates the minimum perimeter stretching factor for which a physically meaningful shape can be fitted.

The lack of shape information in the PIP shape-fitting equations does not entirely explain the artificial cap in aspect ratio at ∼0.6 for the PIP-fitted ellipses, however. If the shape issues were the sole cause of the artificial cap, the circular presentation
420 of particle (d) in Fig. 6 would produce a very good fit with an aspect ratio approaching one. Instead, the aspect ratio cap is a result of where the aspect ratio is most sensitive to the perimeter length for a given particle area. Based on Fig. 7a, the PIP-fitted ellipse major and minor axis lengths and aspect ratio show the greatest sensitivity to perimeter length when the perimeter stretching factor is almost one (i.e., the particle is almost a perfect circle). As a result, any deviation from the smooth edge of a perfect circle will produce relatively rapid changes in the ellipse axis length and the aspect ratio. It was noted above
425 that the PIP-fitted ellipse measurements appear to produce an artificial cap on aspect ratio of approximately 0.6. Based on our calculations for Fig. 7, a PIP-fitted ellipse aspect ratio of 0.6 is produced when the perimeter stretching factor is approximately 1.065 despite our hypothetical particle being circular (i.e., having an aspect ratio of 1.0). For a circular particle with a radius of 0.5 mm (giving a perimeter of ∼3.14 mm), a perimeter stretching factor of 1.065 corresponds to the addition of approximately 0.2 mm to the particle perimeter when performing a PIP-ellipse fit.
430 The PIP-fitted rectangle long- and short-side lengths (Fig. 7b) have a similar sensitivity to changes in perimeter stretching factor when the perimeter stretching factor is relatively small. A key difference from the PIP-fitted ellipses, however, is that a rectangle cannot be fit to a particle whose perimeter stretching factor is less than $\sqrt{4/\pi}$ (∼1.128), below which the particle perimeter is not long enough to construct a rectangle of the required area. Particle (d) in Fig. 6 is an example of a particle
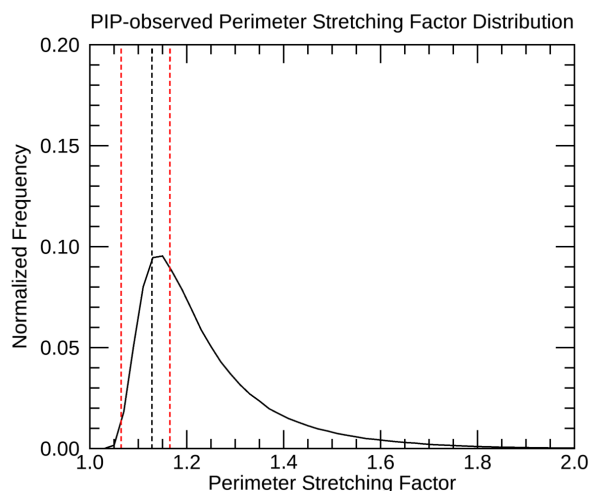
Figure 8. Distribution of perimeter stretching factors computed from PIP observations collected during the 7–8 March 2018 snow event. The two red vertical dashed lines indicate the perimeter stretching factor corresponding to an aspect ratio of 0.6 for a (left red dashed line) PIP-fitted ellipse and (right red dashed line) PIP-fitted rectangle. The black vertical dashed line indicates the smallest perimeter stretching factor that will permit a physically meaningful rectangle fit. Only particles with an area of at least 0.5 mm^2 are included in the histogram.

whose actual perimeter is too short to produce a physical rectangle fit using the PIP method. The perimeter stretching factor

435 for particle (d) is approximately 1.068, as listed in Table 1. Based on this and similar particles, the PIP processing algorithm appears to automatically assign an aspect ratio of one to any particle where a rectangle fit is not physically possible. How the PIP algorithm determines a dimension length in these cases, however, remains unclear.

  The artificial cap in aspect ratio that appears for the PIP-fitted ellipses (Fig. 5a) does not appear to be present in the aspect ratio distributions for the PIP-fitted rectangles (Fig. 5b). A key factor that leads to this difference is demonstrated in Fig. 7b: a

440 rectangle aspect ratio of 0.6 corresponds to a perimeter stretching factor of ∼1.165 compared to 1.065 for a PIP-fitted ellipse. The importance of this perimeter stretching factor difference of 0.1 comes down to the distribution of particle perimeters relative to their areas. Figure 8 depicts the distribution of perimeter stretching factors for the 7–8 March 2018 case. Only a very small portion of particles have a perimeter stretching factor smaller than 1.065 (left red dashed line, Fig. 8) whereas the most frequently observed perimeter stretching factors are smaller than the 1.165 perimeter stretching factor that corresponds to the

445 0.6 aspect ratio for a PIP-fitted rectangle.

5.3 2DVD and PIP bounding-box measurements

Because 2DVD does not instantaneously capture full images of a particle, a 'long dimension versus short dimension' aspect ratio is not computed by the instrument. Instead, 2DVD reports the 'oblateness' of a particle, defined as the aspect ratio of the horizontal width of a particle versus its vertical height. For each camera, the oblateness is computed as the bounding-box height

450 divided by the bounding-box width. An overall oblateness is then computed from the two single-camera oblateness values by
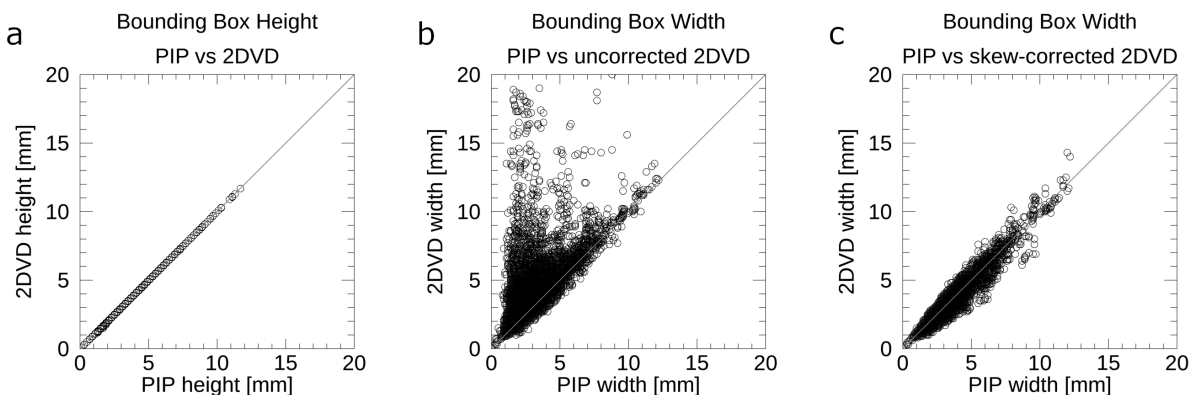
Figure 9. Scatter plots comparing the PIP and 2DVD measurements of (a) bounding-box height and (b,c) bounding-box width with the uncorrected 2DVD-measured width depicted in (b) and the corrected 2DVD-measured width depicted in (c). Only particles with a PIP-measured area of at least 5 mm^2 are included in the plots. All data points are plotted with open circles.

their geometric mean. Here we will focus on the measurements of the bounding box height and width rather than the oblateness itself.

Both PIP and 2DVD record measurements of the horizontal and vertical extent of a particle in the form of bounding-box measurements, computed as the horizontal distance between the left-most and right-most particle pixels and the vertical dis-

455 tance between the bottom-most and top-most particle pixels. Because PIP takes measurements using two-dimensional images, the accuracy of the PIP bounding-box measurements is directly tied to the resolution of the camera and the degree of motion blurring. 2DVD, however, uses a line-scan camera and, as such, the 2DVD bounding-box measurements are derived quantities. The bounding-box height is derived from the time required for the particle to pass through sampling region while the bounding-box width is computed by compositing the individual line scans to rebuild the particle. As discussed in section 3.3, 2DVD uses

460 an unskewing algorithm to correct the bounding-box width measurements for horizontal particle motion. As the actual 2DVD unskewing algorithm is part of a proprietary software package, we use a conceptually similar unskewing algorithm, described in section 4.2.

The vertical sampling frequency of the emulated 2DVD images is usually much higher than that of the underlying PIP images due to the high temporal sampling frequency of 2DVD. In order for the vertical sampling frequency of the emulated

465 2DVD images to be lower than that of the underlying PIP images, the precipitation particle would need to have a fall speed greater than $\sim$68.2 m s^{-1}, which is unrealistic for any of the particles of interest. Because of this, we would expect the emulated 2DVD bounding-box height to almost exactly match the PIP-measured bounding-box height and this expectation is borne out in the data as depicted in Fig. 9a.

Of greater interest is how well the emulated 2DVD bounding-box width measurements perform, especially after we apply our

470 approximation of the 2DVD unskewing algorithm. Figure 9b compares the uncorrected emulated 2DVD bounding-box width with the PIP-measured bounding-box width. Unsurprisingly, the uncorrected 2DVD measurements tend to greatly overestimate

the width of the bounding box due to the skewing introduced by any horizontal motion of the particle. One point of interest, however, is that the uncorrected 2DVD measurements can sometimes underestimate the bounding box width. This can occur when a particle of sufficiently low aspect ratio is moving in the opposite direction of the tilt of the top of the particle (e.g., a needle crystal whose top is to the left of the particle centroid moving towards the right); this will result in the particle being compressed in the horizontal.

The emulated 2DVD measurements of bounding-box width are surprisingly accurate once our approximation of the 2DVD unskewing algorithm is applied (Fig. 9c). After the correction, the overestimation of bounding-box width is considerably reduced compared to the uncorrected emulated 2DVD measurements. The underestimation of bounding-box width that was present with the uncorrected measurements, however, is more common after the correction. The increase in underestimation is due to the assumption that the top-most and bottom-most pixels of the 2DVD-imaged particle are supposed to be vertically aligned with one another. This assumption is frequently broken by snow particles and an example of this assumption resulting in a very minor underestimation of bounding-box width can be seen in Fig. 1.

6   Conclusions

The present study set out to evaluate the measurement techniques used by PIP, MASC, and 2DVD to characterize the size and shape of snowflakes in terms of area, equivalent diameter, and aspect ratio. This was accomplished by using imagery collected by a PIP instrument during the ICE-POP 2018 field campaign to emulate the relevant measurements made by MASC and 2DVD. More specifically, a comparison was made between the ellipse- and rectangle-fitting algorithms used by PIP and the ellipse-fitting algorithm used by MASC; a tensor-based ellipse-fitting algorithm was also evaluated along-side the PIP and MASC shape-fitting algorithms. Additionally, measurements of the bounding-box width and height made by PIP were compared to the emulated 2DVD width and height measurement in order to evaluate the performance of 2DVD when measuring snow particles. The key findings of our comparative evaluation are listed below.

– The 2DVD camera setup should provide the most accurate measure of area (and equi-area diameter) due to its resilience to motion blurring; that said, the relatively low pixel resolution means that the 2DVD area and equi-area diameter measurements should also have low precision (section 5.1).

– The very high resolution MASC cameras should provide the greatest precision in area measurements; despite being susceptible to motion blurring, the MASC cameras should also produce the most accurate measurements of area and equivalent diameter (section 5.1).

– Although the PIP camera setup is slightly more resilient to motion blurring than MASC, the application of an image compression algorithm that involves vertically averaging pixels means that the PIP measurements of area and equivalent diameter are slightly less accurate than MASC and can potentially have a relatively low precision similar to that of 2DVD (section 5.1).

- The MASC ellipse-fitting algorithm produces reasonable ellipse fits of the particles and, as such, produces reliable aspect ratios (section 5.2).

505   – The PIP shape-fitting algorithms do not perform well due to their reliance on only the area and perimeter of a particle; this renders the following variables unreliable: 'Ellip_Maj', 'Ellip_Min', 'Rec_BS', and 'Rec_SS' (section 5.2); other variables reported by the PIP are unaffected by the shape-fitting issues.

- The tensor-based ellipse fitting algorithm performed comparably to the MASC ellipse-fitting algorithm; as such, any aspect ratio measurements using this algorithm should be reliable (section 5.2).

510   – Our implementation of the 2DVD unskewing algorithm, designed to remove the effects of horizontal motion from the 2DVD bounding-box-width measurements, performed surprisingly well with snow particles considering the instrument was designed to measure rain drops (section 5.3). That said, the corrected bounding-box-width measurements are still prone to error due to the motion skewing effects. We expect that the actual implementation of this algorithm should have a similar level of performance.

515   These results suggest that all three instruments have applications for studying snow, albeit with differing degrees of effectiveness. The two-dimensional images collected by MASC and PIP are ideal for measuring snow as they are not susceptible to the skewing produced by the horizontal motion of a particle that is experienced by 2DVD. That said, the very short exposure time of the 2DVD camera effectively results in complete immunity to motion blur, making any measurements of two-dimensional projected particle area highly accurate. Despite the high accuracy of the 2DVD area measurements, its inability to measure the
520 maximum dimension or aspect ratio of a particle (outside of horizontally or vertically oriented particles) limits the usefulness of its measurements.

    The appropriateness of PIP and MASC for characterizing snowflakes largely comes down to the planned application for the data. The very high resolution imagery produced by MASC is ideal for determining ice particle habit, something that is impractical using the low-resolution PIP imagery. PIP, however, captures considerably more particles than MASC does and
525 this greater particle count makes PIP better suited to constructing particle distributions than MASC. Unfortunately, the PIP shape-fitting routines do not perform well on precipitation particles and, as a result, the maximum dimension and aspect ratio measurements are unreliable; however, the PIP variables other than the ellipse and rectangle dimensions appear to be reliable. As a result, any non-shape-fitting-derived values (e.g., Pettersen et al., 2020) will also remain reliable. As the present study has demonstrated, the PIP imagery can be reprocessed and reliable measurements of maximum dimension and aspect ratio can be
530 made via the application of an alternative ellipse-fitting algorithm, such as the MASC or tensor-based algorithms.

Data availability. Bliven, Larry . 2020. GPM Ground Validation Precipitation Imaging Package (PIP) ICE POP. Dataset available online from the NASA Global Hydrology Resource Center DAAC, Huntsville, Alabama, U.S.A. DOI:

    http://dx.doi.org/10.5067/GPMGV/ICEPOP/PIP/DATA101

Appendix A: Derivation of shape-fitting equations for PIP

535   According to the IMAQ Vision concepts manual (National Instruments, 2000), the equations to fit either an ellipse or a rectangle can be derived from the equations for area and perimeter. The area and perimeter equations for a rectangle are, respectively,

$$A = ab \quad \text{and} \tag{A1}$$

$$P = 2\left(a + b\right), \tag{A2}$$

540   where A is the actual particle area, P is the actual particle perimeter, and a and b are the lengths of the long and short sides of the fitted rectangle. For an ellipse, PIP uses the following equations for area and perimeter, respectively:

$$A = \pi ab \quad \text{and} \tag{A3}$$

$$P = \pi\sqrt{2\left(a^2 + b^2\right)}, \tag{A4}$$

545   where the major axis length is equal to $2a$ and the minor axis length is equal to $2b$. Note, the equation PIP uses for the perimeter of an ellipse is actually an upper bound on the perimeter of an ellipse rather than an actual estimate of the perimeter (Jameson, 2014).

   The derivation for the equations used to compute the dimensions of both the PIP-fitted ellipse and rectangle proceed similarly: solving the area equation for either a or b and substituting the result into the perimeter equation. This substitution

550   is followed by putting the resulting equation into the standard form for a quadratic equation for the rectangle and a quartic equation for the ellipse. The standard form quadratic equation for the rectangle fit is

$$0 = -x^2 + \frac{P}{2}x - A, \tag{A5}$$

where x is either a or b depending on the variable for which the area equation was solved. Similarly, the standard form quartic equation for the ellipse fit is

555   $$0 = -\pi^2 x^4 + \frac{P^2}{2}x^2 - A^2. \tag{A6}$$

Note that the IMAQ Vision concepts manual incorrectly records the standard form equation for the ellipse fit as being identical to that of the rectangle fit.

   The standard form equations for both the rectangle- and ellipse-fits can then be solved for their roots. As the ellipse-fit equation is a biquadratic special case of a quartic equation, it can be solved using the same method as a quadratic equation

560   by substituting $z = x^2$, determining the roots, and then substituting $x = \pm\sqrt{z}$ into those roots. Solving both equations via the these methods gives roots of

$$x = \frac{P}{4} \pm \frac{\sqrt{\frac{P^2}{4} - 4A}}{2} \tag{A7}$$

Table B1. List of relevant variables within PIP data files for the reprocessing PIP AVI video files.

Variable	file	Description
recnum	_a_p.dat, _a_v_1.dat, _a_v_2.dat	Record number of particle measurement, unique within each 10-minute period
Q, R	_a_p.dat	Frame index split into two numbers, unique within each 10-minute period.
x_cent, y_cent	_a_p.dat	PIP-measured particle centroid location in pixels
vel_v_1, vel_v_2	_a_v_1.dat, _a_v_2.dat	PIP-measured particle vertical fall speed in m s^{-1}

for the PIP-fitted rectangle and

$$x = \pm\sqrt{\frac{P^2}{4\pi^2} \pm \frac{\sqrt{\frac{P^4}{4} - 4\pi^2 A^2}}{2\pi^2}} \tag{A8}$$

565   for the PIP-fitted ellipse. The only physically meaningful roots will be the positive roots. In the case of the quartic ellipse
equation, one of the positive roots will give the value of a and the other will give the value of b. The other dimension for the
rectangle fit can be computed by plugging the positive root into the equation for area and solving for the unknown dimension
length (either a or b).

Appendix B: PIP video file processing

570   The following builds on section 4 by further discussing the steps taken to reprocess the PIP video files in order to produce
the emulated MASC and tensor fits as well as the emulated 2DVD measurements. Reprocessing the PIP video files for the
alternative fits requires four sets of files: the AVI video files, the '_a_p.dat' particle table files, the '_a_v_1.dat' velocity table
files, and the '_a_v_2.dat' velocity table files. The two velocity table files cover different sets of particles: the '_a_v_1.dat'
files contain data for particles that were only observed in two consecutive frames while the '_a_v_2.dat' files contain data for
575   all particles that were observed in three or more consecutive frames. Using both files maximizes the number of particles that
we can use to make emulated 2DVD measurements. Each AVI file corresponds to one of each of the '.dat' files, although the
'.dat' files typically cover a much greater period of time than what is depicted in the AVI files. The key '.dat' file variables for
the reprocessing algorithm are listed in Table B1.

   The PIP AVI videos include both the PIP view as well as a header that indicates which PIP unit recorded the observations,
580   the time stamp, a combined 'Q_R' frame index, and the number of the frame within the AVI video file (Fig. B1). The key to
matching a single frame of the AVI file to the data contained within the '.dat' files is matching the single-number 'Q_R' frame
index depicted in the video to the two-number 'Q' and 'R' frame index listed in the '_a_p.dat' files; 'Q_R' can be computed
as 'Q' times 32767 plus 'R'. To obtain the 'Q_R' frame index from the video image, we constructed a simple image matching
algorithm. The image matching algorithm compares, via subtraction, the image of each digit of the 'Q_R' frame index to a set
585   of images of individual digits that were previously cropped from PIP AVI videos. A matched digit should result in a difference
of zero, although we selected the digit that produces the smallest difference and allowed for a difference of up to 100, noting
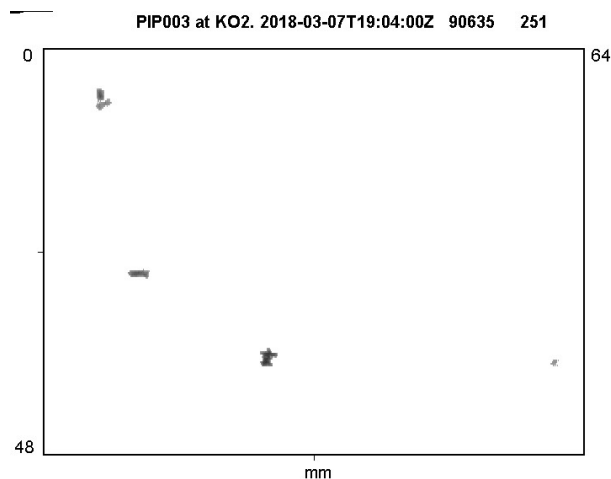
Figure B1. Snapshot taken from a PIP AVI video file collected by the PIP located at the MHS site during ICE-POP. The header can be decoded as follows: 'PIP003 at KO2' indicates which PIP recorded the file, '2018-03-07T12:04:00Z' is the time stamp, '90635' is the 'Q_R' frame index within the current 10-minute period, and '251' is the frame number within this specific AVI file.

that the 'Q_R' frame index can be between one and six digits long and each additional digit shifts the position of all the numbers in the frame by several pixels.

Once the 'Q_R' frame index is determined from the video file and it has been matched to the 'Q' and 'R' frame index in the
590 '_a_p.dat' file, the record number ('recnum') in the '_a_p.dat' file can be matched to the record number in the '_a_v_1.dat' and '_a_v_2.dat' velocity table files. Note, only a subset of particles listed in the '_a_p.dat' file will have matching entries in the velocity table files. Following the above method, we should now have the centroid location and fall speed of each particle in a given frame of the PIP AVI video file. The centroid is used to identify all pixels within a particle, as described in section 4, and the fall speed is used to emulate the 2DVD measurements, as described in section 4.2.

595 *Author contributions.* Dr. Helms led this research by developing and running the code to reprocess the PIP video files, implementing the various measurement algorithms, and performing the various analyses. Dr. Munchak and Dr. Tokay provided input on the methods used in the study and, critically, tested the reprocessed PIP data for quality purposes. Dr. Pettersen provided data support and advice on reprocessing the PIP images.

Competing interests. Some authors are members of the editorial board of Atmospheric Measurement Techniques. The peer-review process
600 was guided by an independent editor, and the authors have also no other competing interests to declare.

Acknowledgements. The authors would like to thank Dr. David Wolff for the fruitful discussions regarding various aspects of this manuscript. Additionally, the authors would also like to thank Drs. Larry Bliven and Jacopo Grazioli for their insights into the inner workings of the PIP and MASC instruments, respectively. The authors are also indebted to the ICE-POP 2018 field campaign participants for their data collection and processing efforts. Dr. Helms' work was supported by an appointment to the NASA Postdoctoral Program at NASA Goddard Space Flight Center, administered by Universities Space Research Association under contract with NASA. Dr. Pettersen's work was supported via NASA grants NASA 80NSSC19K0712 and NASA 80NSSC21K0931.

References

Fitzgibbon, A. W. and Fisher, R. B.: A Buyer's Guide to Conic Fitting., in: Proceedings of the British Machine Vision Conference, pp. 513–522, BMVA Press, doi:10.5244/C.9.51, 1995.

610 Garrett, T. J., Fallgatter, C., Shkurko, K., and Howlett, D.: Fall speed measurement and high-resolution multi-angle photography of hydrometeors in free fall, Atmos. Meas. Tech., 5, 2625–2633, https://doi.org/10.5194/amt-5-2625-2012, 2012.

Grecu, M., Olson, W. S., Munchak, S. J., Ringerud, S., Liao, L., Haddad, Z., Kelly, B. L., and McLaughlin, S. F.: The GPM Combined Algorithm, J. Atmos. Oceanic Technol., 33, 2225–2245, https://doi.org/10.1175/JTECH-D-16-0019.1, 2016.

Han, M. and Braun, S. A.: Understanding the Global Three-dimensional Distribution of Precipitation Mean Particle Size with the Global

615 Precipitation Measurement Mission, J. Climate, 0, 0–0, https://doi.org/10.1175/JCLI-D-21-0134.1, 2021.

Heymsfield, A. J. and Westbrook, C. D.: Advances in the estimation of ice particle fall speeds using laboratory and field measurements, J. Atmos. Sci., 67, 2469–2482, https://doi.org/10.1175/2010JAS3379.1, 2010.

Huang, G.-J., Bringi, V. N., Cifelli, R., Hudak, D., and Petersen, W. A.: A methodology to derive radar reflectivity-liquid equivalent snow rate relations using C-band radar and a 2D video disdrometer, J. Atmos. Oceanic Technol., 27, 637–651,

620 https://doi.org/10.1175/2009JTECHA1284.1, 2010.

Jameson, G.: Inequalities for the perimeter of an ellipse, The Mathematical Gazette, 98, 227–234, https://doi.org/10.1017/S002555720000125X, 2014.

Korolev, A. and Isaac, G.: Roundness and Aspect Ratio of Particles in Ice Clouds, J. Atmos. Sci., 60, 1795–1808, https://doi.org/10.1175/1520-0469(2003)060<1795:RAAROP>2.0.CO;2, 2003.

625 Kruger, A. and Krajewski, W. F.: Two-Dimensional Video Disdrometer: A description, J. Atmos. Oceanic Technol., 19, 602–617, 2002.

Lee, G. and Kim, K.: International Collaborative Experiments for PyeongChang 2018 Olympic and Paralympic winter games (ICE-POP 2018), in: AGU Fall Meeting, American Geophysical Union, San Francisco, CA, 2019.

Leinonen, J., Grazioli, J., and Berne, A.: Reconstruction of the mass and geometry of snowfall particles from multi angle snowflake camera (MASC) images, Atmos. Meas. Tech. Discuss., 0, 0–0, https://doi.org/10.5194/amt-2021-176, 2021.

630 Lim, K.-S. S., Chang, E.-C., Sun, R., Kim, K., Tapiador, F. J., and Lee, G.: Evaluation of simulated winter precipitation using WRF-ARW during the ICE-POP 2018 field campaign, Weather and Forecasting, 35, 2199–2213, https://doi.org/10.1175/WAF-D-19-0236.1, 2020.

Locatelli, J. D. and Hobbs, P. V.: Fall speeds and masses of solid precipitation particles, J. Geophys. Res., 79, 2185–2197, https://doi.org/10.1029/JC079i015p02185, 1974.

Matrosov, S. Y., Heymsfield, A. J., and Wang, Z.: Dual-frequency radar ratio of nonspherical atmopsheric hydrometeors, Geophys. Res. Lett.,

635 32, L13 816, https://doi.org/10.1029/2005GL023210, 2005.

Munchak, S. J., Schrom, R. S., Helms, C. N., and Tokay, A.: Snow Microphysical Retrieval from the NASA D3R Radar During ICE-POP 2018, Atmos. Meas. Tech. Discuss., https://doi.org/10.5194/amt-2021-264, in review, 2021.

National Instruments: IMAQ Vision Concepts Manual, National Instruments, [Available online at https://www.ni.com/pdf/manuals/322916a.pdf], 2000.

640 Newman, A. J., Kucera, P. A., and Bliven, L. F.: Presenting the snowflake video imager (SVI), J. Atmos. Oceanic Technol., 26, 167–179, https://doi.org/10.1175/2008JTECHA1148.1, 2009.

Pettersen, C., Bliven, L. F., von Lerber, A., Wood, N. B., Kulie, M. S., Mateling, M. E., Moisseev, D. N., Munchak, S. J., Petersen, W. A., and Wolff, D. B.: The Precipitation Imaging Package: Assessment of microphysical and bulk characteristics of snow, Atmosphere, 11, 785, https://doi.org/10.3390/atmos11080785, 2020.

645 Pettersen, C., Bliven, L. F., Kulie, M. S., Wood, N. B., Shates, J. A., Anderson, J., Mateling, M. E., Petersen, W. A., von Lerber, A., and Wolff, D. B.: The precipitation imaging package: Phase partitioning capabilities, Remote Sensing, 13, 2183, https://doi.org/10.3390/rs13112183, 2021.

Schönhuber, M., Lammer, G., and Raneu, W. L.: One decade of imaging precipitation measurement by 2D-video-distrometer, Adv. Geosci., 10, 85–90, 2007.

650 Schönhuber, M., Lammer, G., and Randeu, W. L.: The 2D-video-distrometer, in: Precipitation: Advances in measurement, estimation and prediction, edited by Michaelides, S., pp. 3–31, Springer, 2008.

Shkurko, K., Garrett, T., and Gaustad, K.: Multi-Angle Snowflake Camera Value-Added Product, DOE/ARM Tech. Rep. DOE/SC-ARM-TR-187, DOE Office of Science Atmospheric Radiation Measurement (ARM) Program, https://doi.org/10.2172/1342901, 2016.

Stuefer, M. and Bailey, J.: Multi-Angle Snowflake Camera Instrument Handbook, DOE/ARM Tech. Rep. DOE/SC-ARM-TR-158, DOE

655 Office of Science Atmospheric Radiation Measurement (ARM) Program, https://doi.org/10.2172/1261185, 2016.

Tapiador, F. J., Villalba-Pradas, A., Navarro, A., García-Ortega, E., Lim, K.-S. S., Ahn, K. D., and Lee, G.: Future directions in precipitation science, Remote Sensing, 13, 1074, https://doi.org/10.3390/rs13061074, 2021.

Testud, J., Oury, S., Black, R. A., Amayenc, P., and Dou, X.: The concept of "normalized" distribution to describe raindrop spectra: A tool for cloud physcics and cloud remote sensing, J. Appl. Meteor., 40, 1118–1140, https://doi.org/10.1175/1520-

660 0450(2001)040<1118:TCONDT>2.0.CO;2, 2001.

Tyynelä, J., Leinonen, J., Moisseev, D., and Nousiainen, T.: Radar Backscattering from Snowflakes: Comparison of Fractal, Aggregate, and Soft Spheroid Models, J. Atmos. Oceanic Technol., 28, 1365–1372, https://doi.org/10.1175/JTECH-D-11-00004.1, 2011.

von Lerber, A., Moisseev, D., Bliven, L. F., Petersen, W., Harri, A.-M., and Chandrasekar, V.: Microphysical properties of snow and their link to Ze-S relations during BAECC 2014, J. Appl. Meteor. Climatol., 56, 1561–1582, https://doi.org/10.1175/JAMC-D-16-0379.1, 2017.

665 Westbrook, C. D.: Rayleigh scattering by hexagonal ice crystals and the interpretation of dual-polarization radar measurements, Quart. J. Roy. Meteor. Soc., 140, 2090–2096, https://doi.org/10.1002/qj.2262, 2014.